Scanning X-ray diffraction on cardiac tissue: automatized data analysis and processing

Jan-David Nicolas,[a] Marten Bernhardt,[a] Andrea Markus,[b] Frauke Alves,[b] Manfred Burghammer[c] and Tim Salditt[a]*

[a]Institut für Röntgenphysik, Georg-August-Universität Göttingen, 37077 Göttingen, Germany, [b]Max-Planck-Institut für Experimentelle Medizin, Hermann-Rein-Straße 3, 37075 Göttingen, Germany, and [c]European Synchrotron Radiation Facility, 71 Avenue des Martyrs, 38043 Grenoble, France. *Correspondence e-mail: tsaldit@gwdg.de

A scanning X-ray diffraction study of cardiac tissue has been performed, covering the entire cross section of a mouse heart slice. To this end, moderate focusing by compound refractive lenses to micrometer spot size, continuous scanning, data acquisition by a fast single-photon-counting pixel detector, and fully automated analysis scripts have been combined. It was shown that a surprising amount of structural data can be harvested from such a scan, evaluating the local scattering intensity, interfilament spacing of the muscle tissue, the filament orientation, and the degree of anisotropy. The workflow of data analysis is described and a data analysis toolbox with example data for general use is provided. Since many cardiomyopathies rely on the structural integrity of the sarcomere, the contractile unit of cardiac muscle cells, the present study can be easily extended to characterize tissue from a diseased heart.

1. Introduction

Classical small-angle X-ray scattering (SAXS) and X-ray diffraction (XRD) studies are well established tools for the characterization of biomolecular matter and biomaterials. High signal levels are achieved in particular with synchrotron radiation, but still largely rely on macroscopic ensemble-averaging. Local distributions of structural properties cannot be accessed with such an approach. For many samples, however, global average in real space leads to a signal, which is difficult to interpret and to model. In practice, this entails a severe restriction of diffraction methods to homogeneous model systems in many biophysical studies. For the case of biological tissues, for example, biological function relies on both a specific and well defined molecular nano-structure as well as an equally well defined cyto-architecture on the micrometer scale. Ideally, both scales should be probed simultaneously. Heart tissue underlying the physiological function of contractility is an excellent example. Classical diffraction studies on muscle (both for skeletal and cardiac muscle) have contributed to the understanding of the sarcomere as the basic structural unit of the myofibrils which make up muscle fibers. However, it is largely unknown how the molecular structure parameters vary within the tissue, in terms of local orientation, strain and variation in filament lattice spacing, and how they correlate to the textures visualized by histological microscopy.

To avoid the loss of information associated with averaging the signal over many heterogeneous areas, samples can be raster scanned with focused synchrotron beams (Kaulich et al., 2011; Fratzl et al., 1997; Holt et al., 2013; Bunk et al., 2009;

research papers
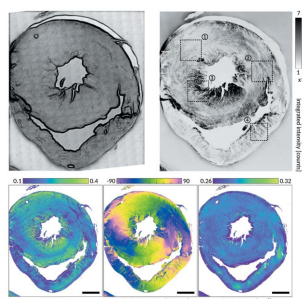
Seidel *et al.*, 2008). However, decreasing the illuminated diffraction volume in each exposure results in a drastic increase in dose or decrease of the signal (or a combination of both). This has been a key challenge in developing X-ray experiments with micro- or nano-focused X-ray probes (Ice *et al.*, 2011), in particular for soft biological samples.

The optics itself required for scanning diffraction experiments has undergone significant progress in recent years. Due to major improvements in the fabrication of focusing optics for hard X-rays, micro- and nano-meter focal spot sizes can now be routinely achieved (Mimura *et al.*, 2010; Vila-Comamala *et al.*, 2012; da Silva *et al.*, 2017). Recent developments in X-ray focusing optics have, for example, been reviewed by Sakdinawat & Attwood (2010). Furthermore, signal-to-noise levels in experiments employing tightly focused beams have improved with the development of novel detection mechanisms for the recording of two-dimensional diffraction patterns (Ryan *et al.*, 2014; Johnson *et al.*, 2012). Finally, accurate sample positioning has been implemented at many synchrotron instruments to generate maps of spectroscopic or scattering parameters, and are widely used for different techniques, for example in transmission X-ray microscopy, scanning X-ray fluorescence microscopy, scanning Bragg diffraction microscopy and X-ray ptychography. Scanning SAXS has also become a routine application, for example in the analysis of textured samples such as teeth (Tesch *et al.*, 2001; Märten *et al.*, 2010; Deyhle *et al.*, 2011, 2014), bone (Wagermaier *et al.*, 2007; Karunaratne *et al.*, 2012; Rinnerthaler *et al.*, 1999; Davies *et al.*, 2008; Gourrier *et al.*, 2010; Granke *et al.*, 2013; Giannini *et al.*, 2014; Bukreeva *et al.*, 2015), wood (Lichtenegger *et al.*, 1999; Müller, 2009; Storm *et al.*, 2015; Merk *et al.*, 2017), silk (Riekel *et al.*, 2017) and polymers (Zafeiropoulos *et al.*, 2005). Extensions to three-dimensional SAXS imaging include 3D-SAXS (Fratzl, 2015; Liebi *et al.*, 2015; Georgiadis *et al.*, 2015; Seidel *et al.*, 2012; Schaff *et al.*, 2015), SAXS-CT (Jensen *et al.*, 2011*a*,*b*) or energy-resolving SAXS (Grünewald *et al.*, 2016). However, as the experiments impose a significant radiation dose onto the sample, scanning SAXS and scanning X-ray diffraction have been largely restricted to strongly scattering materials (where the beam can be attenuated) or to materials which are comparatively radiation insensitive, such as bone for example.

In this work, we show that by combination of moderate focusing, fast scanning, sufficient distance between the illuminated points, background reduction and optimized detection, scanning SAXS and scanning X-ray diffraction become compatible with soft radiation-sensitive biological tissues. As an example and proof-of-concept, we describe scanning X-ray diffraction experiments performed on an entire cardiac tissue slice. With scanning strategy and instrumentation cleverly chosen, meaningful signals can be recorded, and high data throughput automatized analysis becomes the main challenge. To this end, we have developed a versatile data-analysis platform to extract multiple order parameters from the scattering data of tissue. We can thus add real space information to classical SAXS and diffraction studies on cardiac tissue (Matsubara, 1980; Reconditi *et al.*, 2017) by tracing order parameters related to the sarcomere structure throughout an entire slice of cardiac tissue.

The article is outlined as follows. Firstly, in §2 the scanning X-ray diffraction experiment on a cardiac tissue slice is described and results are discussed. Next, in §3, methods for automated data treatment in scanning diffraction experiments are presented. The article closes with a summary and conclusion in §4. An example dataset and a description of the general layout of the data analysis platform is given in Appendix *A*. Data analysis software written in the programming language *MATLAB* (Mathworks Inc., USA) is available online to be used by the scientific community.

2. Scanning X-ray diffraction on cardiac tissue

2.1. Experiment

Data on cardiac tissue were collected at the ID13 endstation (microbeam hutch) of the European Synchrotron Radiation Facility (ESRF, Grenoble, France). The workflow of the scanning diffraction experiment is shown in Fig. 1. Cardiac tissue was obtained from an excised mouse heart. After excision, the heart was embedded in agarose [4% in phospate-buffered saline (PBS)] and cut in a vibratome (VT1000 S, Leica Biosystems, Germany) to a thickness of 30 µm. Prior to the experiment, the sample was mounted between two thin polypropylene foils and a small volume of PBS was added to prevent drying of the sample. The photon energy for the experiment was set to 13.45 keV using a Si(111) channel-cut monochromator. Beam-defining slits and a compound refractive lens (CRL) transfocator were tuned to focus the beam to an elliptical spot size of 2 µm (h) × 3 µm (v). The total photon flux was $I_0 = 1.6 \times 10^{12}$ photons s^{-1}. The sample was aligned using an on-axis video microscope that can be moved laterally with respect to the beam. A tailor-made beamstop housed in a flight tube flushed with helium was used at a distance of approximately 10 cm behind the sample stage to block the primary beam and to reduce background. The scattering patterns were recorded at equal time steps during scanning using an Eiger 4M detector, placed 918 mm downstream of the sample. Note that, in contrast to standard raster scanning of the sample through the beam focus, here the sample was moved continuously at a constant speed during data acquisition. This scheme of continuous scanning was indispensable to cover large tissue areas at tolerable scan time.

2.2. Results

Since the goal of the present study was to image the entire cardiac tissue slice, a total sample area of approximately 6 mm × 5 mm had to be covered. To this end, a total of 1090 (h) × 1331 (v) scan points, an exposure time of 10 ms and a step size of 5 µm were chosen to image the entire tissue. Since the sample was illuminated continuously and moved at a constant speed, the step size is the distance covered between the start of adjacent exposures. In total, data collection took 8 h and 10 min. With a 10 ms exposure time, this resulted in a scan overhead of approximately 10 ms per scan point.
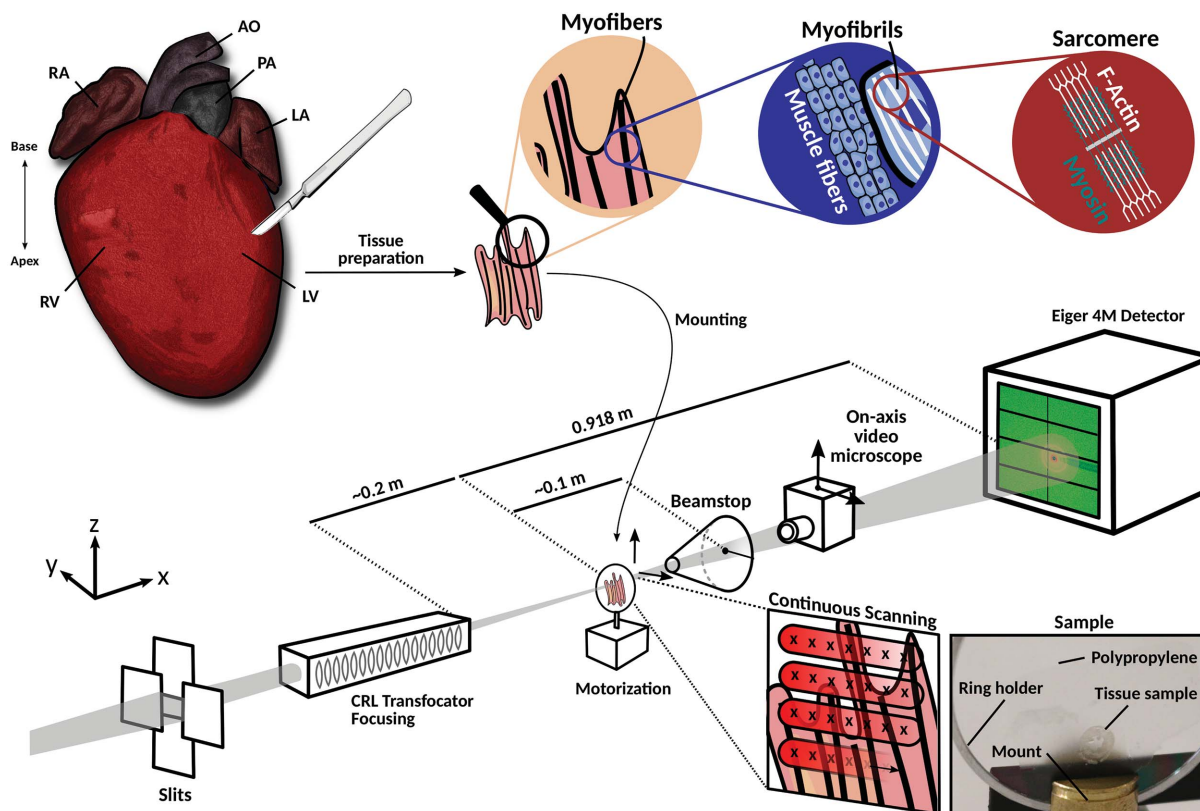
Figure 1
Sketch of the scanning diffraction experiment on tissues. A 30 μm-thick tissue slice from an excised mouse heart, embedded in an agarose matrix, was mounted on a thin polypropylene foil and placed into the focus of the X-ray beam. Zoomed illustrations depict the highly regular arrangement of cardiac muscle fibres. Monochromated undulator radiation is focused down to micrometer spot size, using CRL transfocator optics. Scattered radiation is detected using a two-dimensional pixelated detector (here Eiger 4M, Dectris, Switzerland). An on-axis video microscope facilitates sample positioning and alignment with respect to the beam focus position. A circular beamstop housed in a helium-flushed flight tube blocks unscattered radiation downstream from the focus position. Finally, the sample is swept through the focus of the beam and diffraction patterns are recorded at regular intervals during scanning. The data are read and analyzed by a custom platform for automized data analysis for scanning diffraction experiments. RA, right artery; LA, left artery; AO, aorta; PA, pulmonary artery; LV, left ventricle; RV, right ventricle.

Given the above parameters, an average dose of 577×10^3 Gy was recieved by the sample per scan point. The dose D was calculated from (Shen *et al.*, 2004)

$$D = \frac{\mu I_0 \tau E_{ph}}{\rho \Delta x \Delta y}, \qquad (1)$$

using tabulated values for the mass attenuation coefficient μ and mass density ρ, where $\mu/\rho = 2.0641 \text{ cm}^2 \text{ g}^{-1}$ (Hubbell & Seltzer, 2004). $\Delta x \Delta y = 36.27 \text{ mm}^2$ corresponds to the overall sample area scanned and $\tau = 29400$ s to the overall scan time during which the beam was impinging on the sample.

The overall data storage of this scan was 1.1 TB (using LZ4 compression). Scattered intensity and anisotropy was analyzed in parallel on a system using eight central processing units (Intel® Xeon® CPU E5-2609, 2.40 GHz; Intel Corporation, Santa Clara, USA). The overall computation time was 11 h, largely limited by the process of file reading.

The result of the scan and an optical micrograph that has been recorded directly after the measurement is shown in Fig. 2. Based on the diffraction data, the anisotropy of the (1,1) reflection as well as the myofibril orientation and the filament spacing of the acto-myosin lattice (Fig. 2c) were extracted by fully automated scripts, as important para-meters of cardiac muscle cyto-architecture. The filament spacing was determined from the maxima of the (1,1) reflection in the structure factor $I(q_r)$, obtained by plotting the diffraction intensity as a function of radial momentum transfer $q_r = (q_y^2 + q_z^2)^{1/2} = (4\pi/\lambda)\sin(\theta)$, where 2θ is the scattering angle between the primary and scattered beam and λ the radiation wavelength. Note that the interfilament spacing $d^{(1,0)}$ is obtained from the position of the (1,1) equatorial reflection by $d^{(1,0)} = \sqrt{3}2\pi/q_r^{(1,1)}$.

To extract anisotropy and orientation from the scattering distribution we have followed the approach described by Bernhardt *et al.* (2017). In short, the anisotropy ω of the scattering distribution is defined as $\omega = |\lambda_1 - \lambda_2|/(\lambda_1 + \lambda_2)$, where λ_1 and λ_2 correspond to the eigenvalues of the covariance matrix of the momentum transfer along q_y and q_z. The filament orientation in this model is defined as the angle of the largest eigenvalue rotated by 90°. To this end, the covariance matrix was determined within a detector region, defined by a suitable mask, in order to avoid contamination of the signal by background scattering close to the beamstop and by the noise floor at high q_r. As indicated in Fig. 5, values of $q_{min} = 0.22 \text{ nm}^{-1}$ and $q_{max} = 0.38 \text{ nm}^{-1}$ were found suitable. Myofibril orientation was color coded as presented by Kovesi (2015).
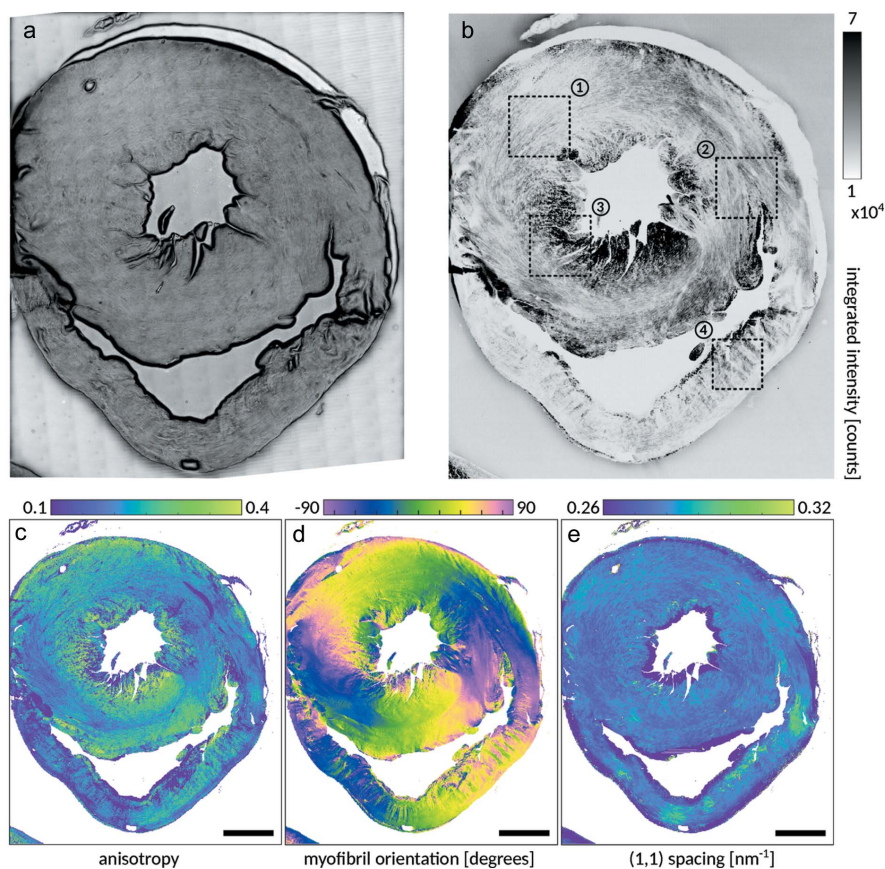
Figure 2
Scanning X-ray diffraction dataset on tissue slices from mouse cardiac muscle. (a) Optical micrograph and scanning diffraction image (darkfield contrast) of a mouse heart. Multiple-scattering parameters are extracted in a fully automated manner, such as (b) integrated scattered intensity, (c) anisotropy of the scattering resulting from the $d^{(1,1)}$ reflection from the acto-myosin lattice, (d) the corresponding myofibril orientation, and (e) the extracted mean position of the reflection along q_r. The mean positions were obtained by fitting a Gaussian and a background model to the structure factor $I(q_r)$. For clarity, background is plotted in white.

marked in Fig. 2(b), each pixel in the ROIs has been analyzed with respect to the following four parameters: integrated scattered intensity, anisotropy, myofibril orientation and interfilament spacing. Some characteristic patterns of the tissue already become apparent in the darkfield maps, representing the local scattering strength of the tissue averaged over all q_r values. From theses micrometer-sized structures, see for example the stripy pattern in ROI 1, preferential directions and tissue orientation can be inferred. We stress, however, that the intrinsic orientation of biomolecular assemblies within the illuminated spot can only be assessed from analyzing the anisotropy. In the current case, this signal is dominated by myofibril orientation. Both the degree of orientation and the principal direction are quantified. Interesting myofibril arrangements can, for example, be observed in ROI 3. Finally, the results show that the interfilament spacing is not constant in all regions, but shows pronounced local variations.

The interfilament spacing is deduced pixel-wise by performing an angular average of the data after background subtraction. The data are fitted by a model function, consisting of two power law decays and a Gaussian distribution describing the $q_r^{(1,1)}$ reflection, i.e. $I(q_r) = aq_r^{-b} + cq_r^{-d} + e\exp[-(q_r - f)^2/\sigma^2]$, where a–f are fit parameters. The reflection width was determined at $\sigma = 0.034\ \mathrm{nm}^{-1}$ and fixed during the fitting process.

To verify that indeed the reflection position is changing with lateral position within the sample, the angular averaged structure factor of three examplary data points A, B and C are depicted together with the respective model function in Figs. 4(a) and 4(b). In general, one could depict the distribution of each fitting parameter in its entirety. To this aim, all fit parameters have been normalized by subtraction of the arithmetic mean and dividing by the standard deviation σ of the respective distribution. Fig. 4(c) visualizes the normalized distribution of the reflection strength (fit parameter e) and reflection position (fit parameter f). Mean and standard deviation of all distributions are tabulated for completeness in Fig. 4(d).

Given the myofibril orientation shown in Fig. 2(d), it becomes apparent that the myofibrils circulate around the left ventricle (LV) of the heart. The anisotropy of the scattering shown in Fig. 2(c) shows that the scattering is more isotropic in the bulk of the muscle. Interestingly, the position of the (1,1) reflection is not constant throughout the tissue, but appears textured with reflection positions as large as 0.3 nm^{-1}, which is significantly larger than the mean value 0.275 nm^{-1} of the present data. Furthermore, around the epi- and endocardium of the heart, the reflection position suddenly shifts to lower values of around 0.25 to 0.26 nm^{-1}. The observed local changes in interfilament spacing might result from an interplay with the surrounding tissue matrix, and cannot be observed in macroscopic diffraction experiments averaging over large muscle regions. Note that the interfilament spacing is known to depend on many physiological parameters, in particular osmotic stress (Konhilas *et al.*, 2002). For a whole (unsliced), perfused and hydrated rat heart, the literature value of $q_r^{(1,1)} = 0.29$ nm^{-1} can be used as a reference (Yagi *et al.*, 2004).

More detailed views of the tissue within selected regions of interest (ROIs) are shown in Fig. 3. Based on the four ROIs

3. Processing and analysis of scanning diffraction data

In the following section, we describe in more detail how scattering data from these scanning experiments were processed and analyzed in a robust, automated and model-independent fashion. Most of the steps are standard proce-
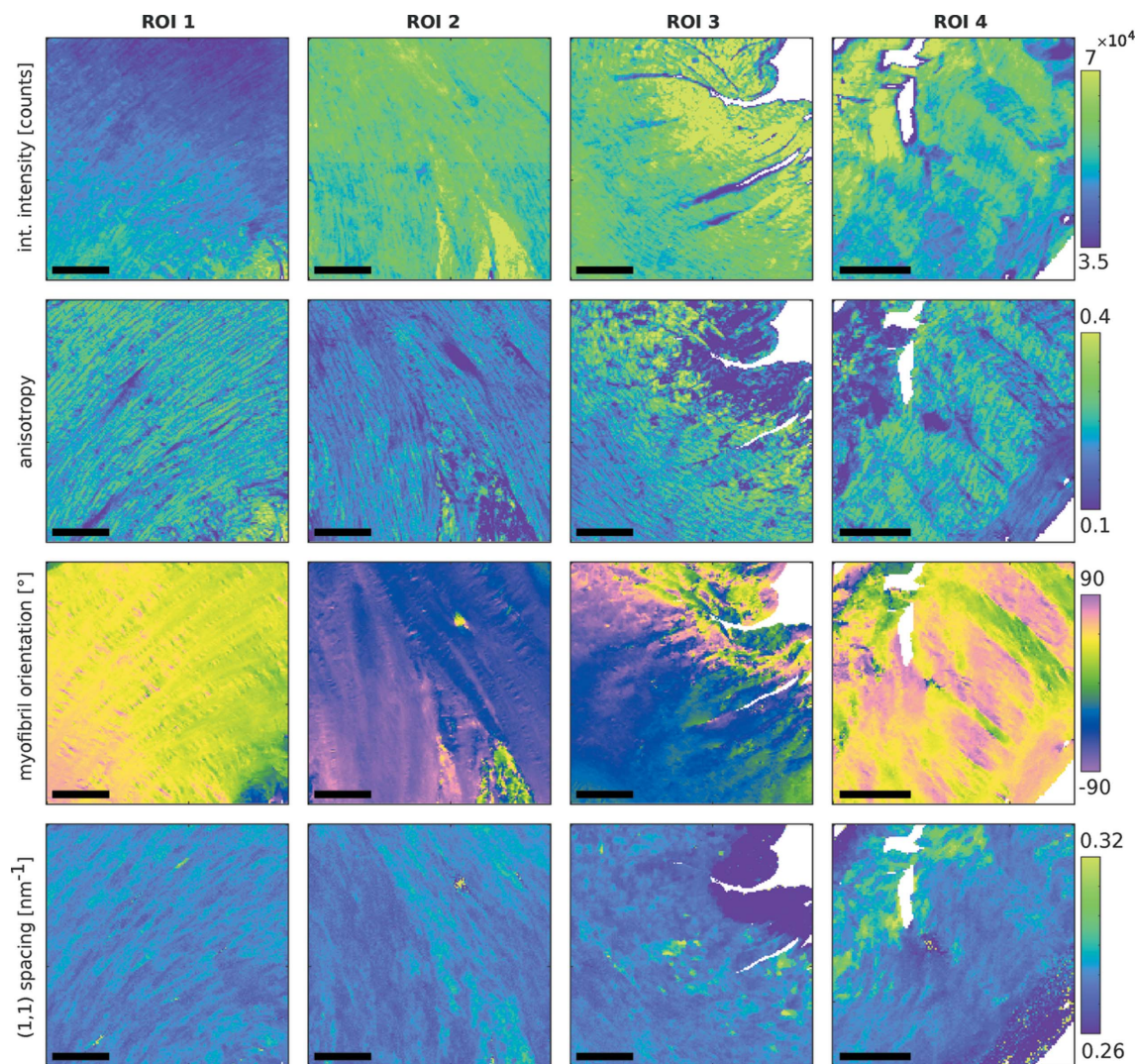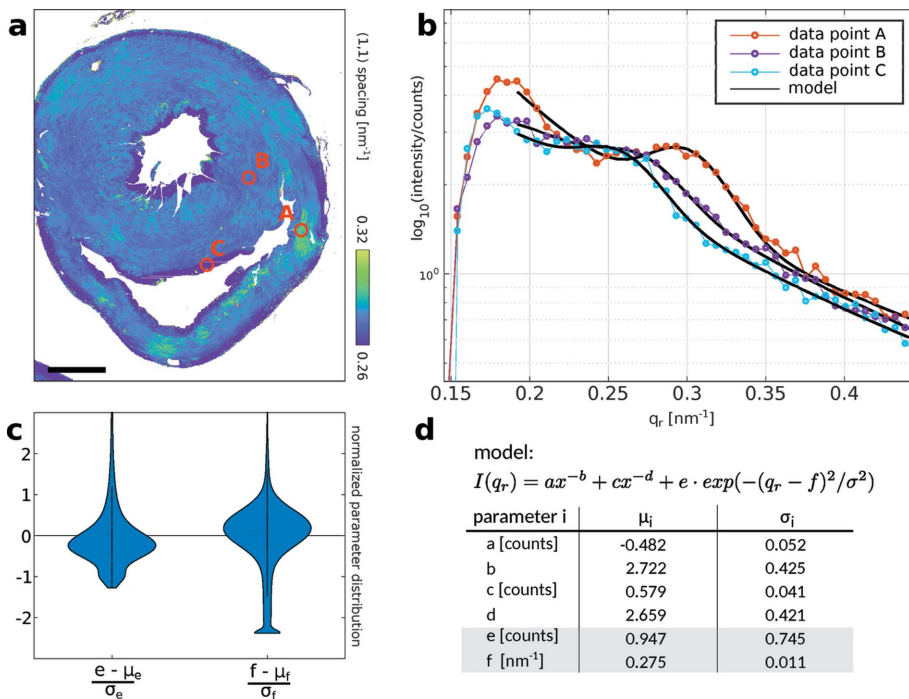
Figure 3
Analysis of darkfield contrast, anisotropy, myofibril orientation and acto-myosin lattice spacing, as in Fig. 2. Regions of interest (ROIs) are marked by black dashed boxes in the overview darkfield map in Fig. 2(*b*). Scale bar: 100 μm.

dures, used in many diffraction experiments, but are described and illustrated for completeness. In particular, we want to stress that a research field which initially was started by analysis software, based on reading in a single diffraction pattern, treated by individual mouse clicks such as in Hammersley (1997), must now be replaced by fully automated and high-throughput scripts. All data processing tasks described here are implemented in the data analysis toolbox. Data analysis tasks not treated in this manuscript are documented in the toolbox.

One major step in data processing of two-dimensional diffraction data is a suitable data pre-processing. Many mistakes can be made, especially by an inexperienced user, in the data masking and data selection. Data masking is the task of identifying incorrect data, that will be neglected in further data processing tasks, while data selection reduces an otherwise valid data set to a desired range of q_r-values and angles, for example to discriminate a signal against background. An example of data masking and data selection is shown in Fig. 5.

A raw diffraction pattern obtained using an Eiger 4M detector is shown in Fig. 5(*a*). Intermodular gaps and hot pixels are represented by 2^{16} counts. It is crucial to mask all invalid pixels by a detector mask depicted in Fig. 5(*b*). Multiplying the raw detector image with the detector mask will result in an image shown in Fig. 5(*c*). Several analysis routines require data originating from within a certain q_r range. A corresponding pixel mask that is later being used for data selection is shown in Fig. 5(*d*). Note that, in addition to defining logical data masks, data can also be selected based on identifying a certain region on the detector and binning the data by an integer fraction, as illustrated in Fig. 5(*e*) with a binning ratio of 4.

Following data pre-processing steps such as masking, selection and binning, the two-dimensional data can be either directly analyzed or mapped to a one-dimensional representation. Common examples are azimuthal and radial integration of the data. Azimuthal integration refers to summing intensities over the azimuthal angle ϕ or a restricted (selectable) angular interval $\Delta\phi$, resulting in a one-dimensional $I(q_r)$

Figure 4
Comparison of scattering profiles and their respective fits from three selected data points on the sample. (*a*) Map of the (1,1) lattice spacing as shown in Fig. 2. Red circles mark the location of the data points A, B and C for which azimuthally integrated structure factor profiles $I(q_r)$ are shown in (*b*) together with the respective fit. A fitting model composed of two power-law decays and a superimposed Gaussian was used to obtain the peak position $q^{(1,0)}$. (*c*) Violin plot of the normalized distributions of the reflection strength $I(q_r^{(1,0)})$ (fit parameter *e*) and respective reflection position $q_r^{(1,0)}$ (fit parameter *f*). The arithmetic mean μ and standard deviation σ of all fit parameters are summarized together with the model function in (*d*).

curve with selectable Δq_r bins. If only a certain angular interval $\Delta\phi$ is evaluated, this is also commonly denoted as cake integration or wedge integration. Contrarily, radial integration refers to summation of intensities over the full radial range or a selected subset of the radial coordinate, yielding $I(\phi)$. The process of $2d \rightarrow 1d$ mapping is sketched in Fig. 6. For this purpose, different algorithmic implementations can be selected based on the users needs for accuracy, robustness or computational speed:

(i) A fast and straightforward approach for azimuthal integration simply rebins the two-dimensional data $I(q_r, \phi)$ in equidistant intervals Δq_r. Formally, this approach can be written as

$$I(b) = \frac{\sum_{(q_r,\phi)} \Pi_b(q_r)\, I(q_r, \phi)}{\sum_{(q_r,\phi)} \Pi_b(q_r)}, \qquad (2)$$

where

$$\Pi_b(q_r) = \begin{cases} 1 & \text{if } b\Delta q_r \le q_r < (b+1)\Delta q_r \\ 0 & \text{otherwise} \end{cases} \qquad (3)$$

identifies all pixels corresponding to a given q_r interval and b is the corresponding integer bin index.

(ii) For more advanced data regridding, the *pyFAI* suite (Kieffer & Karkoulis, 2013) can be used. Since *pyFAI* is a computational library for azimuthal regridding written in

the Python programming language, it is natively supported in the *MATLAB* code used here.

In comparison, a simple azimuthal rebinning is faster than the basic azimuthal integration implementation (using the *NumPy* package for data processing). Since computational speed is of major concern, data regridding should be parallelized so that calculations can be distributed on multiple central processing units or the graphics processing unit.

4. Summary and conclusion

The experiment demonstrates that heart tissue slices can be mapped by scanning diffraction with high data throughput based on continuous scanning and fast pixel detector read-out. In particular, the entire (small animal) heart cross section can be covered in one scan, at still sufficiently fine (micrometer-sized) sampling. Plotting the result of such a diffraction scan, the signal level of the X-ray scattering provides an X-ray darkfield contrast for the tissue, which already reflects the cyto-architecture of the tissue slices quite well. By automated analysis of the local diffraction pattern, we have further shown that the local filament orientation and lattice parameter, *i.e.* characteristic spacing of actin and myosin filaments in myofibrils, can be extracted by automated data analysis. Furthermore, not only the direction but also the degree of orientational order can be quantified. Scanning diffraction of muscle tissue is thus complementary to macroscopic muscle diffraction experiments which average over large ensembles, since they allow the biomolecular structure to be correlated with the local cyto-architecture. Interestingly, we have found pronounced local variations in the acto-myosin lattice parameter. Rather than strain in crystalline materials, where here such variations in lattice spacing reflect the local stress, such variations must occur in development (assembly) of tissue, and must be interpreted with respect to mechanical functions. In this way, we are convinced that the demonstrated approach can further advance cariovascular research, which has taken ample advantage of synchrotron radiation (Yagi *et al.*, 2004; Shirai *et al.*, 2013; Matsubara *et al.*, 1989). However, only now has different technological progress enabled scanning and analysis of large tissue areas with micrometer-sized sampling, single-photon-counting pixel detectors and automated diffraction analysis.

At first sight, after more than two decades of progress in scanning micro- and nano-diffraction, the present scanning diffraction study of tissue may seem rather standard from a
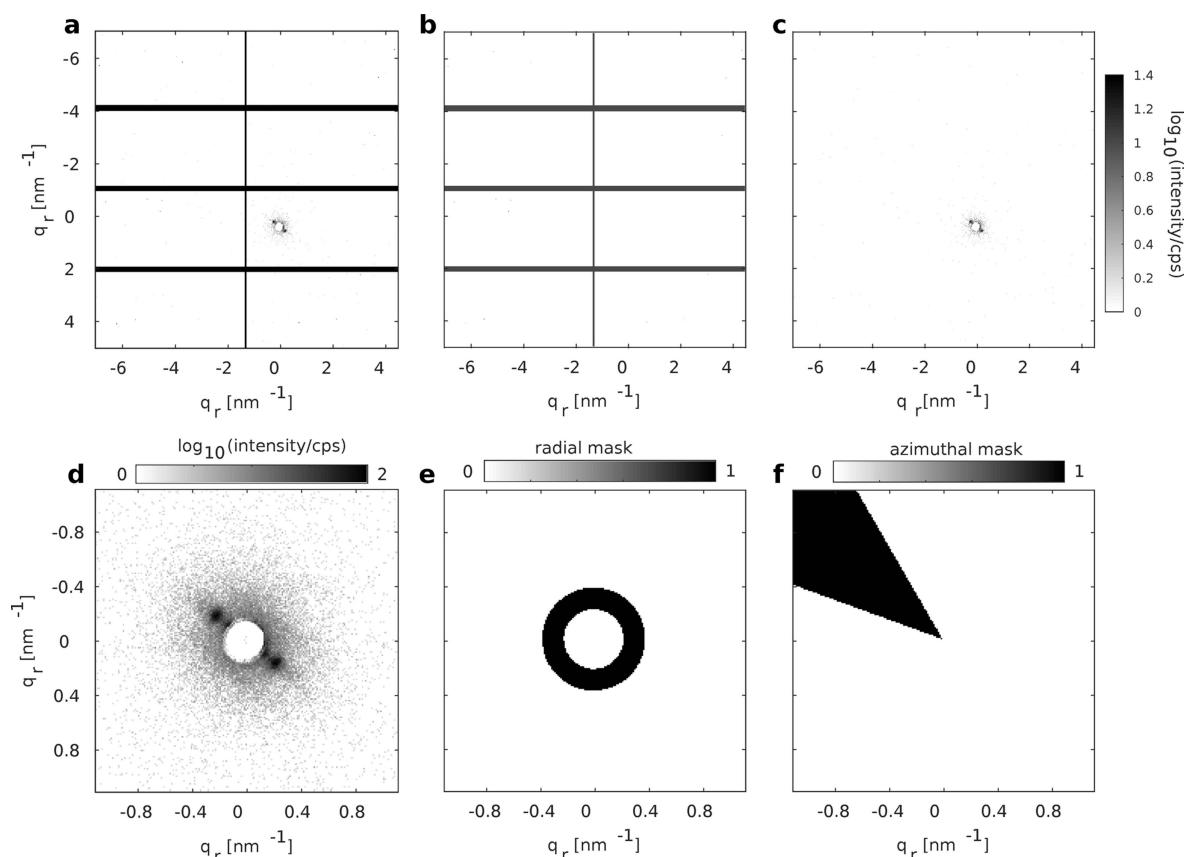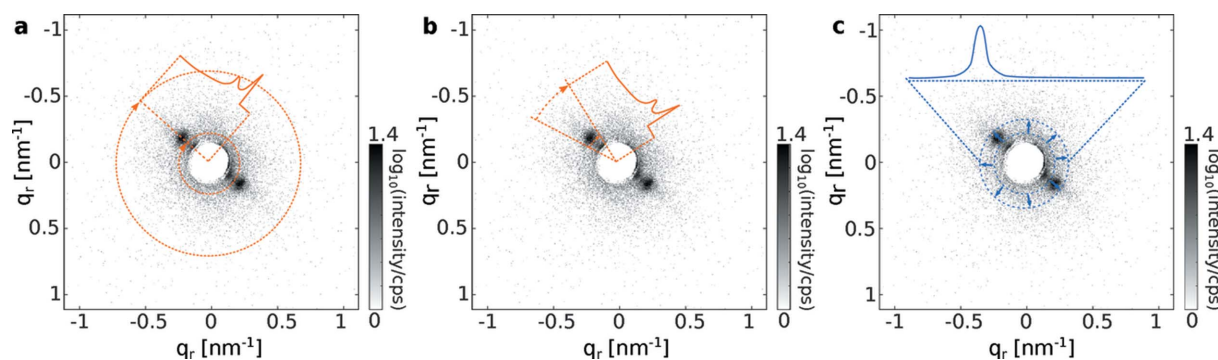
Figure 5
Options for pre-processing of diffraction data. Shown in (*a*) is a raw detector image recorded with an Eiger 4M detector. Modular gaps and hot pixels are represented by 2^{16} counts. By defining a logical mask for hot pixels, modular gaps and the beamstop area (*b*), the masked pixels are set to zero in the diffraction pattern (*c*). (*d*) In addition, ROIs can be defined and data can be binned by binning factors $i \in \mathbb{N}$ along each dimension (here, binning factor 2 along each dimension). (*e*) Radial mask defining a range from 0.22 nm^{-1} to 0.38 nm^{-1} and (*f*) azimuthal mask ranging from 120 to 160°.

conceptional or even technical point of view. However, we must keep in mind that, concerning biological samples and in particular tissues, scanning diffraction is to date largely restricted to strongly scattering and in particular mineralized tissues, such as bone or wood, materials for which the technique was initially developed (Lichtenegger *et al.*, 1999; Fratzl, 2003; Fratzl & Weinkamer, 2007). To date, much fewer studies on wet and soft tissues than on hard tissue have been published. This is for a good reason, as such experiments face two main challenges: firstly, low signal-to-noise due to a weak

diffraction signal, and, secondly, an inherent sensitivity to radiation damage.

The first issue requires improvements of the optical scheme, involving optimized focusing and background reduction, but also of the analysis, since weak signals often necessitate careful pre-processing of the data and analysis schemes. At the same time, meaningful results often require larger scan areas to verify whether signals are representative and correlate with optical microscopy. While this is true for most samples, it becomes vital for weak signals, which are often more difficult

Figure 6
Several 2D → 1D mappings should be routinely feasible in scanning diffraction experiments. (*a*) Full azimuthal integration, (*b*) azimuthal integration within an angular range ('cake integration') and (*c*) radial integration within a certain q_r range.

to interpret in practice. As a result, high-throughput data recording and analysis is required. With progress in instrumentation (pixel detectors, beamline control and continuous scanning) and in analysis (automated scripts and algorithms, compatibility with large data volume), this has now become possible.

The second issue is more difficult. In the present example, the strategy was as simple as efficient: short exposure (10 ms), micrometer-sized focal spot (2–3 μm) and a step size approximately two times larger than the spot size, so that always a fresh part of the sample was exposed. In other words, real-space resolution was deliberately sacrificed by choosing a micro-focused rather than a nano-focused beam. This has three advantages. Firstly, it helps to obtain a cleaner beam profile and lower background, resulting in a higher resolution in reciprocal space. Secondly, the lower flux density helps to avoid beam damage. Thirdly, larger volumes, in this case an entire slice of mouse heart, can be scanned. With the chosen parameters, the structural results are (at least not visibly) affected by radiation damage, and high throughput and sensitivity could be achieved for the important case of cardiac tissue. In principle, multiple sections of a mouse heart making up a full heart in three dimensions could be scanned by this approach. Furthermore, the present study can easily be performed on tissue from a diseased heart, since many cardiomyopathies have their origin in the sarcomere (Lopes & Elliott, 2014). As an example, the interplay of the muscular tissue with the surrounding matrix, *e.g.* in cardiac fibrosis, can be studied.

One may be tempted to concede that cardiac tissue with its regular acto-myosin structure and parallel micro-filaments is more ordered than other tissues and may therefore be exceptionally amenable to diffraction studies, similar to biological materials such as wood and bone. However, many other tissues also exhibit high and interpretable signal levels, including for example the central and peripheral nervous system, related to the myelin sheath around axons. In the case of brain tissue, scanning diffraction might also be a valuable tool in the study of protein aggregations in neurodegenerative diseases. We are therefore convinced that the particular combination of fast scanning methods in combination with a fast acquisition scheme implemented now at many beamlines, as well as improvements in optics (focusing, background reduction) in combination with novel automated analysis tools, now make scanning diffraction applicable to soft biological tissues. The technique can complement standard histology and established microscopy techniques with additional contrast and structural information.

While the entire workflow from sample preparation and mounting to beam shaping, selection of scan parameters and detection scheme are equally important, we stress in this work in particular the role of automated analysis given the nowadays vastly increased amount of data generated during scanning diffraction experiments. To this end, we have presented a straightforward but numerically efficient approach. The custom-made data analysis platform for scanning diffraction experiments as well as an example data set have been made available online or can be obtained by the authors on demand.

APPENDIX *A*
Data analysis toolbox and example data

A1. Data analysis toolbox

Data analysis software can often facilitate access to unexperienced users of an experimental technique. Small-angle X-ray scattering is a great example of how powerful analysis tools can increase accessibility and collaboration between research fields. In the case of scanning X-ray diffraction, much progress has been made in establishing software methods for X-ray data analysis. However, due to the diverse nature of the scattering signal to be expected from inhomogeneous samples, data analysis requires a more flexible set of tools.

In order to analyze data from multiple beamlines in a robust fashion, we have developed a *MATLAB*-based toolbox for data analysis. The toolbox consists of three separate modules to separate data reading from data processing and visualization, as sketched in Fig. 7. The overall structure was chosen to have data-related tasks separated syntactically; however, key functionality is also accessible *via* stand-alone methods that are not bound to a certain module. All methods are designed to make simple tasks easy and complex tasks possible. The toolbox is available on GitHub (https://irpgoe.github.io/nanodiffraction/). A detailed documentation can be found in the internal documentation.

Finally, we believe that the described toolbox can contribute well to the analysis of arbitrary scanning diffraction data, alongside more complex data analysis suites, such as *DAWN 2* (Filik *et al.*, 2017), *DPDAK* (Benecke *et al.*, 2014), *SMC* (Davies, 2006) or *MMW-I* (Bergamaschi *et al.*, 2016), that most often base their workflow on a graphical user interface. Hence, the described toolbox should be understood as a means to simplify data analysis of arbitrary data. A clean syntax should make it easy to understand and use offline or online, during an experiment, even for users with little background in computer programming. More experienced users should also easily be able to add new data analysis methods.

A2. Example dataset and visualization

An example dataset obtained at the ID13 nanohutch endstation on a similar sample has been made available online at Zenodo (Nicolas *et al.*, 2017), that can be used to test the functionality of the data analysis toolbox. The example data set and a representative PCA analysis of the data is shown as an example in Fig. 8. Example code (including calibrated experimental parameters) for these data is provided in the data analysis toolbox.
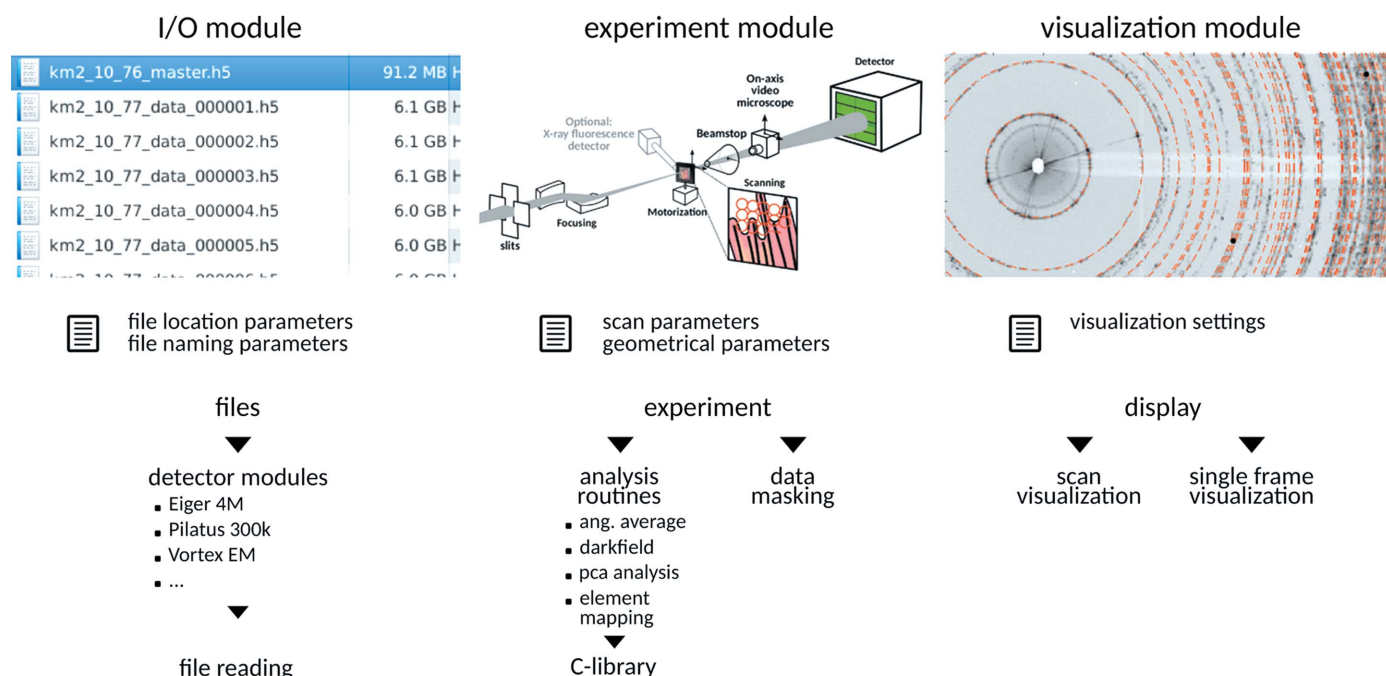
Acknowledgements

Figure 7
Illustration of the modular design approach and workflow of the proposed data analysis toolbox for scanning diffraction experiments. Data treatment is separated into three main tasks: data reading, analysis and visualization. The I/O module 'files' is initialized with parameters related to the file storage and naming conventions used, and file reading routines are contained for each detector in a seperate module. Data can be requested by the experiment module that contains parameters of the experiment and can perform standard analysis procedures in a batch processing manner. Finally, parameter maps or single frames can be easily visualized by the 'display' module.
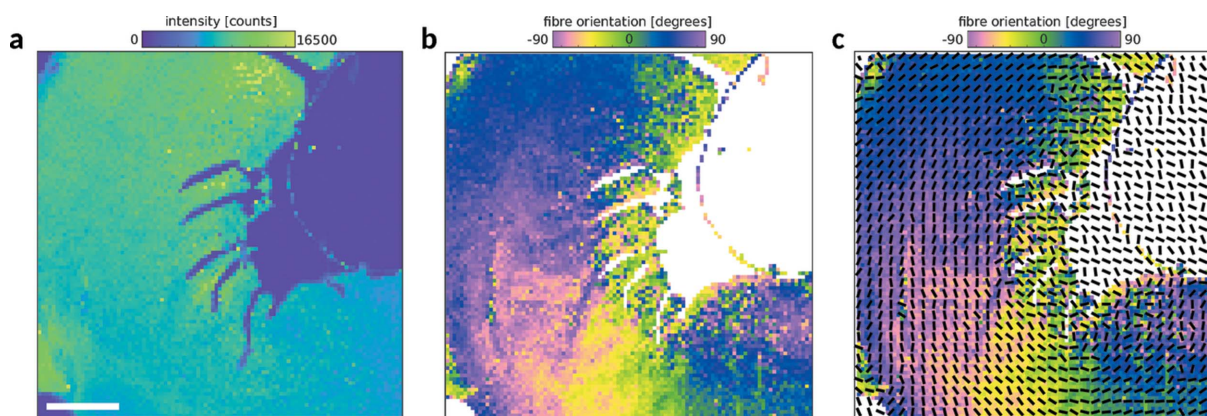

Figure 8
Example dataset. Integrated scattered intensity and fibre orientation are shown in (*a*) and (*b*), respectively. Note that, besides color scaling, a quiver plot (*c*) might be a reasonable choice to visualize orientations. Scale bar: 400 μm.

References

Benecke, G., Wagermaier, W., Li, C., Schwartzkopf, M., Flucke, G., Hoerth, R., Zizak, I., Burghammer, M., Metwalli, E., Müller-Buschbaum, P., Trebbin, M., Förster, S., Paris, O., Roth, S. V. & Fratzl, P. (2014). *J. Appl. Cryst.* **47**, 1797–1803.

Bergamaschi, A., Medjoubi, K., Messaoudi, C., Marco, S. & Somogyi, A. (2016). *J. Synchrotron Rad.* **23**, 783–794.

Bernhardt, M., Nicolas, J.-D., Eckermann, M., Eltzner, B., Rehfeldt, F. & Salditt, T. (2017). *New J. Phys.* **19**, 013012.

Bukreeva, I., Fratini, M., Campi, G., Pelliccia, D., Spanò, R., Tromba, G., Brun, F., Burghammer, M., Grilli, M., Cancedda, R., Cedola, A. & Mastrogiacomo, M. (2015). *Front. Bioeng. Biotechnol.* **3**, 133.

Bunk, O., Bech, M., Jensen, T. H., Feidenhans'l, R., Binderup, T., Menzel, A. & Pfeiffer, F. (2009). *New J. Phys.* **11**, 123016.

Davies, R. J. (2006). *J. Appl. Cryst.* **39**, 267–272.

Davies, R. J., Koenig, C., Burghammer, M. & Riekel, C. (2008). *Appl. Phys. Lett.* **92**, 101903.

Deyhle, H., Bunk, O. & Müller, B. (2011). *Nanomedicine: Nanotechnol. Biol. Med.* **7**, 694–701.

Deyhle, H., White, S. N., Bunk, O., Beckmann, F. & Müller, B. (2014). *Acta Biomater.* **10**, 355–364.

research papers

Filik, J., Ashton, A. W., Chang, P. C. Y., Chater, P. A., Day, S. J., Drakopoulos, M., Gerring, M. W., Hart, M. L., Magdysyuk, O. V., Michalik, S., Smith, A., Tang, C. C., Terrill, N. J., Wharmby, M. T. & Wilhelm, H. (2017). *J. Appl. Cryst.* **50**, 959–966.

Fratzl, P. (2003). *Curr. Opin. Colloid Interface Sci.* **8**, 32–39.

Fratzl, P. (2015). *Nature (London)*, **527**, 308–309.

Fratzl, P., Jakob, H. F., Rinnerthaler, S., Roschger, P. & Klaushofer, K. (1997). *J. Appl. Cryst.* **30**, 765–769.

Fratzl, P. & Weinkamer, R. (2007). *Prog. Mater. Sci.* **52**, 1263–1334.

Georgiadis, M., Guizar-Sicairos, M., Zwahlen, A., Trüssel, A. J., Bunk, O., Müller, R. & Schneider, P. (2015). *Bone*, **71**, 42–52.

Giannini, C., Siliqi, D., Ladisa, M., Altamura, D., Diaz, A., Beraudi, A., Sibillano, T., De Caro, L., Stea, S., Baruffaldi, F. & Bunk, O. (2014). *J. Appl. Cryst.* **47**, 110–117.

Gourrier, A., Li, C., Siegel, S., Paris, O., Roschger, P., Klaushofer, K. & Fratzl, P. (2010). *J. Appl. Cryst.* **43**, 1385–1392.

Granke, M., Gourrier, A., Rupin, F., Raum, K., Peyrin, F., Burghammer, M., Saïed, A. & Laugier, P. (2013). *PLoS One*, **8**, e58043.

Grünewald, T. A., Rennhofer, H., Tack, P., Garrevoet, J., Wermeille, D., Thompson, P., Bras, W., Vincze, L. & Lichtenegger, H. C. (2016). *Angew. Chem.* **128**, 12376–12381.

Hammersley, A. P. (1997). ESRF Internal Report ESRF97HA02T. ESRF, Grenoble, France.

Holt, M., Harder, R., Winarski, R. & Rose, V. (2013). *Annu. Rev. Mater. Res.* **43**, 183–211.

Hubbell, J. H. & Seltzer, S. M. (2004). *Tables of X-ray Mass Attenuation Coefficients and Mass Energy Absorption Coefficients*, v. 1.4. Gaithersburg: National Institute of Standards and Technology. http://physics.nist.gov/xaamdi.

Ice, G. E., Budai, J. D. & Pang, J. W. L. (2011). *Science*, **334**, 1234–1239.

Jensen, T., Bech, M., Bunk, O., Menzel, A., Bouchet, A., Duc, G. L., Feidenhans'l, R. & Pfeiffer, F. (2011a). *NeuroImage*, **57**, 124–129.

Jensen, T. H., Bech, M., Bunk, O., Thomsen, M., Menzel, A., Bouchet, A., Le Duc, G., Feidenhans'l, R. & Pfeiffer, F. (2011b). *Phys. Med. Biol.* **56**, 1717–1726.

Johnson, I., Bergamaschi, A., Buitenhuis, J., Dinapoli, R., Greiffenberg, D., Henrich, B., Ikonen, T., Meier, G., Menzel, A., Mozzanica, A., Radicci, V., Satapathy, D. K., Schmitt, B. & Shi, X. (2012). *J. Synchrotron Rad.* **19**, 1001–1005.

Karunaratne, A., Davis, G., Hiller, J., Esapa, C., Terrill, N., Brown, S., Cox, R., Thakker, R. & Gupta, H. (2012). *Bone*, **51**, 553–562.

Kaulich, B., Thibault, P., Gianoncelli, A. & Kiskinova, M. (2011). *J. Phys. Condens. Matter*, **23**, 083002.

Kieffer, J. & Karkoulis, D. (2013). *J. Phys. Conf. Ser.* **425**, 202012.

Konhilas, J. P., Irving, T. C. & de Tombe, P. P. (2002). *Circ. Res.* **90**, 59–65.

Kovesi, P. (2015). *arXiv*:1509.03700.

Lichtenegger, H., Müller, M., Paris, O., Riekel, C. & Fratzl, P. (1999). *J. Appl. Cryst.* **32**, 1127–1133.

Liebi, M., Georgiadis, M., Menzel, A., Schneider, P., Kohlbrecher, J., Bunk, O. & Guizar-Sicairos, M. (2015). *Nature (London)*, **527**, 349–352.

Lopes, L. R. & Elliott, P. M. (2014). *Heart*, **100**, 1916–1923.

Märten, A., Fratzl, P., Paris, O. & Zaslansky, P. (2010). *Biomaterials*, **31**, 5479–5490.

Matsubara, I. (1980). *Annu. Rev. Biophys. Bioeng.* **9**, 81–105.

Matsubara, I., Maughan, D. W., Saeki, Y. & Yagi, N. (1989). *J. Physiol.* **417**, 555–565.

Merk, V., Berg, J. K., Krywka, C. & Burgert, I. (2017). *Cryst. Growth Des.* **17**, 677–684.

Mimura, H., Handa, S., Kimura, T., Yumoto, H., Yamakawa, D., Yokoyama, H., Matsuyama, S., Inagaki, K., Yamamura, K., Sano, Y., Tamasaku, K., Nishino, Y., Yabashi, M., Ishikawa, T. & Yamauchi, K. (2010). *Nat. Phys.* **6**, 122–125.

Müller, M. (2009). *Mater. Sci. Forum*, **599**, 107–125.

Nicolas, J.-D., Bernhardt, M., Markus, A., Alves, F., Burghammer, M. & Salditt, T. (2017). *Scanning X-ray diffraction data on cardiac tissue. Zenodo*, https://doi.org/10.5281/zenodo.1027712.

Reconditi, M., Caremani, M., Pinzauti, F., Powers, J. D., Narayanan, T., Stienen, G. J. M., Linari, M., Lombardi, V. & Piazzesi, G. (2017). *Proc. Natl Acad. Sci. USA*, **114**, 3240–3245.

Riekel, C., Burghammer, M., Dane, T. G., Ferrero, C. & Rosenthal, M. (2017). *Biomacromolecules*, **18**, 231–241.

Rinnerthaler, S., Roschger, P., Jakob, H. F., Nader, A., Klaushofer, K. & Fratzl, P. (1999). *Calcif. Tissue Int.* **64**, 422–429.

Ryan, C. G., Siddons, D. P., Kirkham, R., Li, Z. Y., de Jonge, M. D., Paterson, D. J., Kuczewski, A., Howard, D. L., Dunn, P. A., Falkenberg, G., Boesenberg, U., De Geronimo, G., Fisher, L. A., Halfpenny, A., Lintern, M. J., Lombi, E., Dyl, K. A., Jensen, M., Moorhead, G. F., Cleverley, J. S., Hough, R. M., Godel, B., Barnes, S. J., James, S. A., Spiers, K. M., Alfeld, M., Wellenreuther, G., Vukmanovic, Z. & Borg, S. (2014). *J. Phys. Conf. Ser.* **499**, 012002.

Sakdinawat, A. & Attwood, D. (2010). *Nat. Photon.* **4**, 840–848.

Schaff, F., Bech, M., Zaslansky, P., Jud, C., Liebi, M., Guizar-Sicairos, M. & Pfeiffer, F. (2015). *Nature (London)*, **527**, 353–356.

Seidel, R., Gourrier, A., Burghammer, M., Riekel, C., Jeronimidis, G. & Paris, O. (2008). *Micron*, **39**, 198–205.

Seidel, R., Gourrier, A., Kerschnitzki, M., Burghammer, M., Fratzl, P., Gupta, H. S. & Wagermaier, W. (2012). *Bioinsp. Biomim. Nanobiomater.* **1**, 123–131.

Shen, Q., Bazarov, I. & Thibault, P. (2004). *J. Synchrotron Rad.* **11**, 432–438.

Shirai, M., Schwenke, D. O., Tsuchimochi, H., Umetani, K., Yagi, N. & Pearson, J. T. (2013). *Circ. Res.* **112**, 209–221.

Silva, J. C. da, Pacureanu, A., Yang, Y., Bohic, S., Morawe, C., Barrett, R. & Cloetens, P. (2017). *Optica*, **4**, 492–495.

Storm, S., Ogurreck, M., Laipple, D., Krywka, C., Burghammer, M., Di Cola, E. & Müller, M. (2015). *J. Synchrotron Rad.* **22**, 267–272.

Tesch, W., Eidelman, N., Roschger, P., Goldenberg, F., Klaushofer, K. & Fratzl, P. (2001). *Calcif. Tissue Int.* **69**, 147–157.

Vila-Comamala, J., Pan, Y., Lombardo, J., Harris, W. M., Chiu, W. K., David, C. & Wang, Y. (2012). *J. Synchrotron Rad.* **19**, 705–709.

Wagermaier, W., Gupta, H. S., Gourrier, A., Paris, O., Roschger, P., Burghammer, M., Riekel, C. & Fratzl, P. (2007). *J. Appl. Cryst.* **40**, 115–120.

Yagi, N., Shimizu, J., Mohri, S., Araki, J., Nakamura, K., Okuyama, H., Toyota, H., Morimoto, T., Morizane, Y., Kurusu, M., Miura, T., Hashimoto, K., Tsujioka, K., Suga, H. & Kajiya, F. (2004). *Biophys. J.* **86**, 2286–2294.

Zafeiropoulos, N. E., Davies, R. J., Roth, S. V., Burghammer, M., Schneider, K., Riekel, C. & Stamm, M. (2005). *Macromol. Rapid Commun.* **26**, 1547–1551.